pubs.acs.org/Biomac

Article

Nanofibrous Peptide Hydrogels Leveraging Histidine to Modulate pH-Responsive Supramolecular Assembly and Antibody Release

Gabriel Saenz,[#] Brett H. Pogostin,[#] Carson C. Cole, Anushka Agrawal, Danielle Chew-Martinez, Marija Dubackic, Antara Pal, Ulf Olsson, Kevin J. McHugh,* and Jeffrey D. Hartgerink*

Cite This: *Biomacromolecules* 2025, 26, 490−502

Read Online

ACCESS | Metrics & More | Article Recommendations | Supporting Information

ABSTRACT: In this work, we investigate the pH-responsive behavior of multidomain peptide (MDP) hydrogels containing histidine. Small-angle X-ray scattering confirmed that MDP nanofibers sequester nonpolar residues into a hydrophobic core surrounded by a shell of hydrophilic residues. MDPs with histidine on the hydrophilic face formed nanofibers at all pH values tested, but the morphology of the fibers was influenced by the protonation state and the location of histidine in the MDP sequence. MDPs with histidine residues within the hydrophobic face disassemble below physiological pH and form nanofibers at higher pH. Taking advantage of their stimulus-triggered behavior, an anti-PD-1 antibody was loaded into histidine MDP hydrogels to examine pH-dependent differences in payload delivery in vitro. Hydrogels composed of MDPs with histidine on the hydrophilic face demonstrated pH-dependent payload retention. Additionally, they showed significantly slower antibody release and reduced antibody diffusion rates in vitro compared to MDP hydrogels lacking histidine.

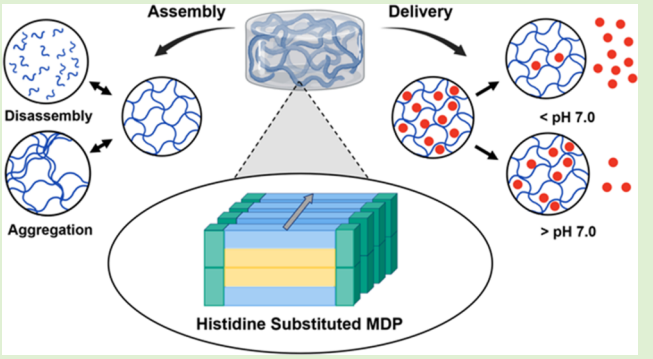

INTRODUCTION

Peptide-based hydrogels are attractive materials for biomedical applications due to their innate biodegradability and tunable mechanical and biological properties.[1−7] These favorable attributes have led to their use in a wide variety of biomedical applications including tissue engineering, wound healing, biosensing, and drug delivery.[8−14] Most peptide hydrogels form via spontaneous self-assembly through noncovalent interactions such as hydrophobic packing, hydrogen bonding, electrostatic, van der Waals, and $\pi-\pi$ stacking. These reversible interactions are highly sensitive to their chemical environment, and therefore, self-assembling peptides must delicately balance attractive and repulsive dynamic interactions between their constituent residues to yield hierarchical secondary and higher-order structures that result in a self-supporting hydrogel. This sensitivity to their chemical environment also allows self-assembling peptide hydrogels to respond to external stimuli, which can be intentionally programmed into the peptide sequence for various applications.[15−17] External stimuli, including pH, temperature, enzymatic activity, and light, have been successfully used to modulate the properties of self-assembling peptide hydrogels; however, pH is the most commonly investigated stimulus due to the naturally occurring pH variations found across organs and between healthy and diseased tissue.[18−22] Previous investigations have leveraged pH-responsive peptide hydrogels to exploit the acidic tumor microenvironment for the controlled release of drug cargo, as well as increase payload retention and efficacy in preclinical cancer models.[23−25]

Peptides are typically engineered with pH-responsive behavior through the incorporation of key functional groups, pH-liable linkers, or charged amino acids. The attachment of pH-labile functional groups, such as *cis*-aconityl, acetals, and dimethylmaleic amides, results in a pH-responsive irreversible chemical change and has been successfully modulated for payload release and drug-induced programmed cell death.[26−31] Conversely, the incorporation of basic and/or acidic amino acids exploits changes in ionization states to create reversible pH triggers in assembly and morphology.[32−34] These reversible pH triggers offer promising potential in the creation of novel delivery systems that adapt to the unpredictable and dynamic pathology of disease progression. Systems relying on irreversibly cleaved linkers could increase undesired side effects in long-term delivery as they fail to adapt to tissue pathology beyond an initial change in pH. Reversible triggers,

Received: September 22, 2024
Revised: December 20, 2024
Accepted: December 20, 2024
Published: December 30, 2024

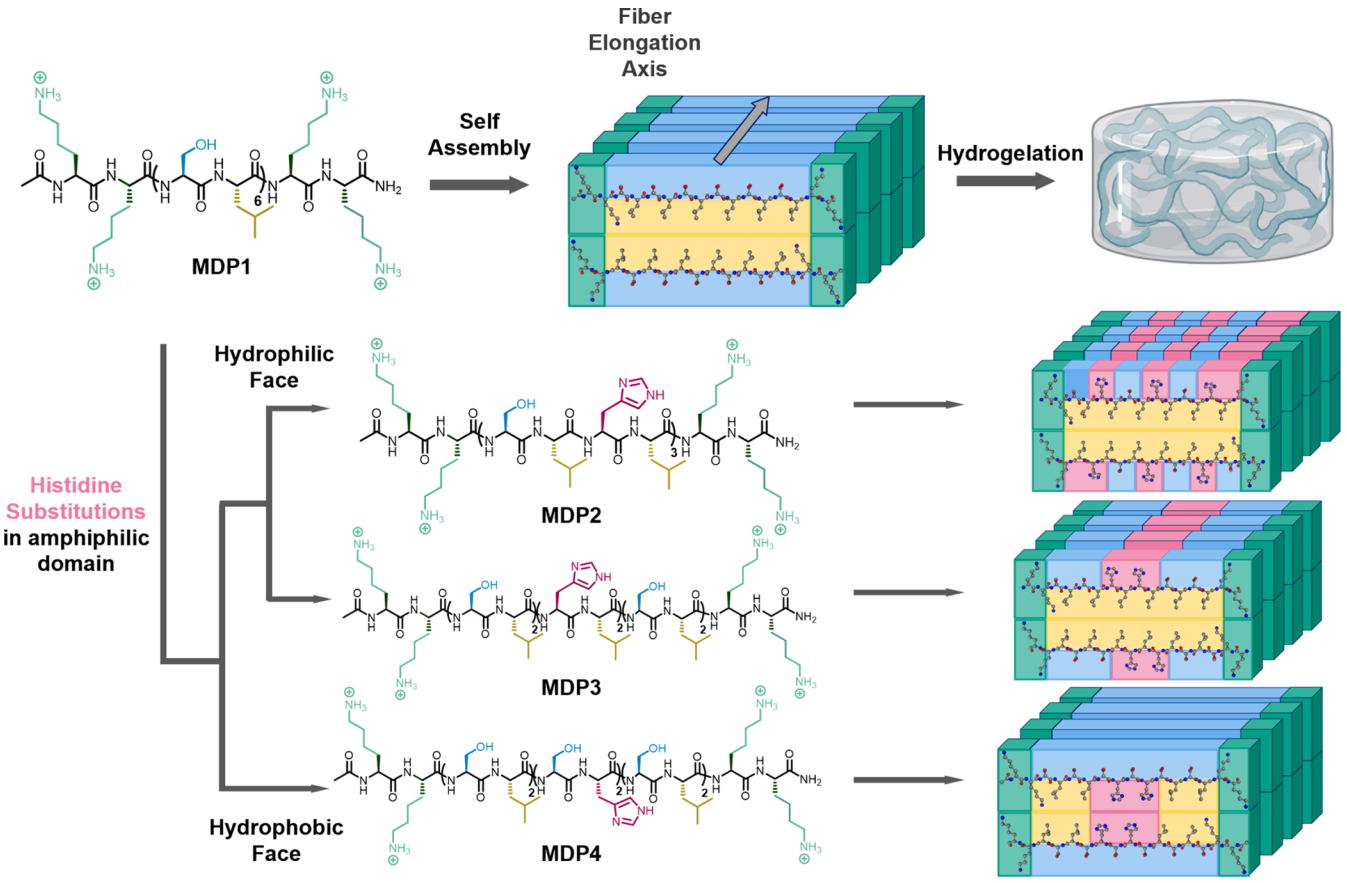

Figure 1. General schematic of multidomain peptide self-assembly mechanism with charged terminals (green), hydrophilic residues (blue), and hydrophobic residues (yellow), as well as the peptides investigated in the current study (MDP2-MDP4) with histidine substitutions marked in pink.

however, can be potentially exploited to continuously respond to stimuli and slow delivery of the therapeutic payload as successful treatment progression stabilizes exogenous pH. Of the charged amino acids, histidine is of particular interest for pH-responsive peptides as the imidazole side chain has a pK_a in the range of 5.5−6.5 that enables changes in protonation state over a physiologically relevant pH range.[35] Notably, histidine plays a significant role in reversible interactions of natural self-assembly processes, such as the pH-triggered confirmational changes observed in cell membrane fusion.[36] Histidine has also been found to impact the structure and self-assembly of abnormally folded amyloid β protein through the contribution of nitrogen donors for Cu (II) and Zn (II) coordination.[37,38] Due to its unique pK_a, histidine is especially well-suited for drug delivery applications, where it can enable pH-responsive drug release. This strategy has been previously exploited in synthetic histidine-containing peptide systems to facilitate the targeted release of therapeutic payloads in diseased tissues, such as tumors where the pH of the microenvironment is near or below the pK_a of histidine.[24,39−41] Similarly, several studies have explored how histidine functionalization disrupts the structural stability of polymeric systems at acidic pH, leading to the extracellular release of encapsulated payloads in tumors.[42−44]

Multidomain peptides (MDPs) are a particular class of hydrogel-forming self-assembling peptides that rely on an ABA motif, wherein the A domains contain charged amino acid residues that flank a central amphiphilic B domain containing alternating hydrophilic and hydrophobic residues.[45] In aqueous solutions, it is believed that the amphiphilic core drives the aggregation of two peptide hydrophobic faces to form a dimer that is frequently termed a "hydrophobic sandwich". These assembled dimers are theorized to associate with other dimers via hydrogen bonding between the backbones of adjacent peptides to form antiparallel β-sheet nanofibers.[46] The flanking charged A termini improve solubility, mediate uniform assembly through the accumulation of electrostatic repulsion, and serve as a handle for fiber cross-linking through the addition of multivalent salts (Figure 1).[47] A 3:1 ratio of hydrophilic−hydrophobic repeats to charged residues has been determined to effectively balance peptide solubility with nanofiber formation.[48] Measurements extrapolated from Cryo-TEM and AFM images of MDP nanofibers have been in good agreement with the proposed "hydrophobic sandwich" assembly model, but further high-resolution experimentation is needed for the direct validation of this bilayer architecture.[45] However, MDP self-assembly is sensitive to the specific amino acid constituents within the amphiphilic domain. For instance, the use of serine in the hydrophilic residue over glutamine resulted in higher storage moduli and shear recovery properties in an otherwise identical MDP sequence.[46] Similarly, strategic placement of aromatic amino acids in the hydrophobic residues resulted in the preferential formation of parallel, not antiparallel, β-sheet structures.[47]

MDP hydrogels are a promising class of biomaterials for clinical translation due to their tunability, injectability, biocompatibility, and capacity to mimic the extracellular matrix.[46,48−51] Their robust design and ease of chemical

https://doi.org/10.1021/acs.biomac.4c01296
Biomacromolecules 2025, 26, 490−502

modification have enabled MDPs to be successfully employed for a variety of preclinical biomedical applications including wound healing, tissue regeneration, and cancer immunotherapy.[50−53] MDP hydrogels have been previously used to prolong the release of a wide variety of functional bioactive materials and proteins.[48] Our lab has successfully used MDPs for the controlled release of biological payloads such as IL-4, MCP-1, VEGF, FGF2, and EGF, while still retaining their biological activity.[10,54,55] The most widely investigated MDP hydrogel for biomedical applications has the structure Ac-KK(SL)$_6$KK-Am (MDP1, Table 1). Changes to the terminal or core residues of this sequence have resulted in various MDPs with unique properties.[56] For instance, a "missing tooth" MDP sequence where a central Leu residue is replaced with Ala was designed to trap small hydrophobic molecules to improve their sustained release.[52]

Table 1. Sequence and Naming Conventions of MDP Peptides Studied Where Ac Represents an N-Terminal Acetylation and Am Represents a C-Terminal Amidation

abbreviation	sequence	residue replaced	no. of histidines
MDP1	Ac-K$_2$(SL)$_6$K$_2$-Am		
MDP2	Ac-K$_2$(SLHL)$_3$K$_2$-Am	serine	3
MDP3	Ac-K$_2$(SL)$_2$(HL)$_2$(SL)$_2$K$_2$-Am	serine	2
MDP4	Ac-K$_2$(SL)$_2$(SH)$_2$(SL)$_2$K$_2$-Am	leucine	2

In this work, we created and evaluated MDPs exhibiting pH-sensitive assembly and nanofiber morphology by substituting serine for histidine in the amphiphilic B domain of MDP1, keeping the charged A domains constant to isolate the effects of histidine (Table 1). Due to histidine's near-neutral pK_a, we hypothesized that these histidine substitutions would introduce a pH-dependent trigger that promotes nanofiber assembly at physiological pH and hydrogel disassembly in acidic environments (Figure 1).[45] We hypothesized that the placement of histidine in the hydrophilic face would affect fiber formation and morphology through the introduction of additional electrostatic repulsion at lower pHs, as well as introduce a new site for noncovalent interaction, such as hydrogen bonding and $\pi-\pi$ stacking (MDP2 and 3). In contrast, the placement of histidine in the hydrophobic peptide face was expected to perturb secondary structure formation at lower pHs when histidine is predominantly found in its protonated state by disrupting the hydrophobic core of the MDP fibers (MDP4). We then explored the use of these new MDPs for the pH-responsive delivery of an anti-PD-1 antibody *in vitro*. Leveraging the strategic placement of histidine on both faces, we found that histidine-modified MDPs form novel pH-responsive nanofibers with diverse morphological, physical, and drug delivery properties. Additionally, by employing small-angle scattering (SAXS) for high-resolution measurements of our nanofiber morphologies, we have also further validated the "hydrophobic sandwich" model of MDP self-assembly with data supporting the formation of a well-ordered hydrophobic core within MDP nanofibers.

EXPERIMENTAL METHODS

Peptide Synthesis. All peptides were synthesized on an Aapttec Focus XC autosynthesizer (Louisville, KY) via standard solid-phase peptide synthesis. Low loading rink amide methylbenzhydryl amine (MBHA) resin and fluorenylmethoxycarbonyl chloride (FMOC)-protected amino acids were supplied by EMD Millipore (Burlington, MA). To deprotect, resin (1 equiv) was shaken in reaction vessel with 25% (v/v) piperidine in 1:1 dimethylformamide (DMF)/dimethyl sulfoxide (DMSO) twice for 5 min each. For each coupling, protected amino acids (4 equiv) were activated with O-(7-azabenzotriazol-1-yl)-*N*,*N*,*N*′,*N*′-tetramethyluronium hexafluorophosphate (HATU) (4 equiv) and N,N-diisopropylethylamine (DiEA) (6 equiv) in 50% DMF/50% DMSO before being added to the resin for 45 min each coupling. N-terminal acetylation was manually performed by adding acetic anhydride (200 equiv) and DiEA (75 equiv) in dichloromethane (DCM) for 45 min two times. Peptides were cleaved from resin using a cleavage cocktail of trifluoroacetic acid (TFA)/anisole/triisopropylsilane/ethane-1,2-dithiol/Milli-Q (MQ) H_2O in a 90: 2.5: 2.5: 2.5: 2.5 ratio for 3 h. TFA was evaporated under a nitrogen stream, and peptides were precipitated with cold ethyl ether.

Peptide Purification. Crude peptide was dissolved to a concentration of 10 mg/mL in a 20% (v/v) solution of acetonitrile in MQ water. Solutions were then purified with high-performance liquid chromatography (HPLC) on a reverse phase XBridge OBD C4 column (Waters Corporation, Milford, MA) with a solvent system of 0.05% TFA in MQ water (Solvent A) and 0.05% TFA in acetonitrile (Solvent B) using a 3%/min gradient from 5−35% Solvent B. Absorbance was monitored at 220 nm with a TUV detector. Solutions were then concentrated *in vacuo*, lyophilized, and stored dry at −20 °C until needed. A Bruker (Billerica, MA) Autoflex matrix-assisted laser desorption/ionization mass spectrometer (MALDI MS) and ultraperformance liquid chromatography (UPLC) were used to confirm peptide identity and purity (Figure S1).

Peptide Gelation. Peptides were dissolved to a concentration of 20 mg/mL in MQ water before adding an equal volume of 2X phosphate-buffered saline (PBS), containing 23.8 mM sodium phosphate dibasic, 23.8 mM potassium phosphate monobasic, 274 mM sodium chloride, and 5.4 mM potassium chloride to create a final 1.00 w/v% peptide solution (10 mg/mL). Solutions were then corrected to the desired pH (±0.05 pH units for each correction) with the addition of NaOH or HCl as needed. The pH of each sample was confirmed using a Seven Excellence S400 pH meter (Mettler Toledo, Colombus, OH). Solutions were vortexed, sonicated, and left at least overnight to form gels (Figure S2).

Circular Dichroism Spectroscopy. Spectra was measured with a Jasco J-810 spectropolarimeter (JASCO Corporation, Tokyo, Japan). Gelled samples were placed in a quartz cuvette with a 0.001 cm path length before recording spectra at room temperature from 250 to 190 nm with a scan rate of 50 nm/min over 5 accumulations (Figure S3). Millidegrees (mdeg) of rotation were converted to mean residue ellipticity (MRE) for ease of comparison using the equation $[\theta] = \theta \times 10^6/(c \times l \times \mathrm{nr})$, wherein c is the concentration (μmol//L), l is the cuvette path length (mm), nr is the number of peptide amino acid residues, and θ is the ellipticity reading in mdeg.

Rheometry. Oscillatory rheology measurements were collected on an AR-G2 rheometer (TA Instruments, New Castle, DE). All hydrogels were prepared at least 12 h in advance. Hydrogel aliquots (75 μL) of each sample were transferred onto the rheometer stage using a truncated 200 μL pipet. A 12 mm stainless steel parallel plate was then lowered onto the sample to a 500 μm gap height. Excess gel was removed from the stage, and mineral oil was applied to prevent evaporation. The storage (G') and loss (G'') moduli were recorded after equilibration at 1 rad/s and 1% strain for 30 min. After equilibration, frequency sweep analysis was performed by subjecting gels to 0.1−10 rad/s at 1% strain (Figure S4). Hydrogels were then allowed to equilibrate for 2 min at 1 rad/s under 1% strain before being sheared at 200% strain for 1 min. Shear recovery was monitored as hydrogels were allowed to equilibrate for 10 min at 1 rad/s at 1% strain (Figure S5). Percent recovery was quantified by comparing the G' values at the end of the 10 min equilibration with the G' values at the end of the initial 2 min equilibration.

Cryo Transmission Electron Microscopy. All gels were prepared as previously described at 1.00 w/v% in PBS buffer. Before plunging, samples were diluted to 0.10 w/v% in fresh MQ water. Samples were prepared on 200 mesh lacey carbon grids. 5 μL of each sample was plunged into liquid ethane with a Leica EM GP automatic

https://doi.org/10.1021/acs.biomac.4c01296
Biomacromolecules 2025, 26, 490−502

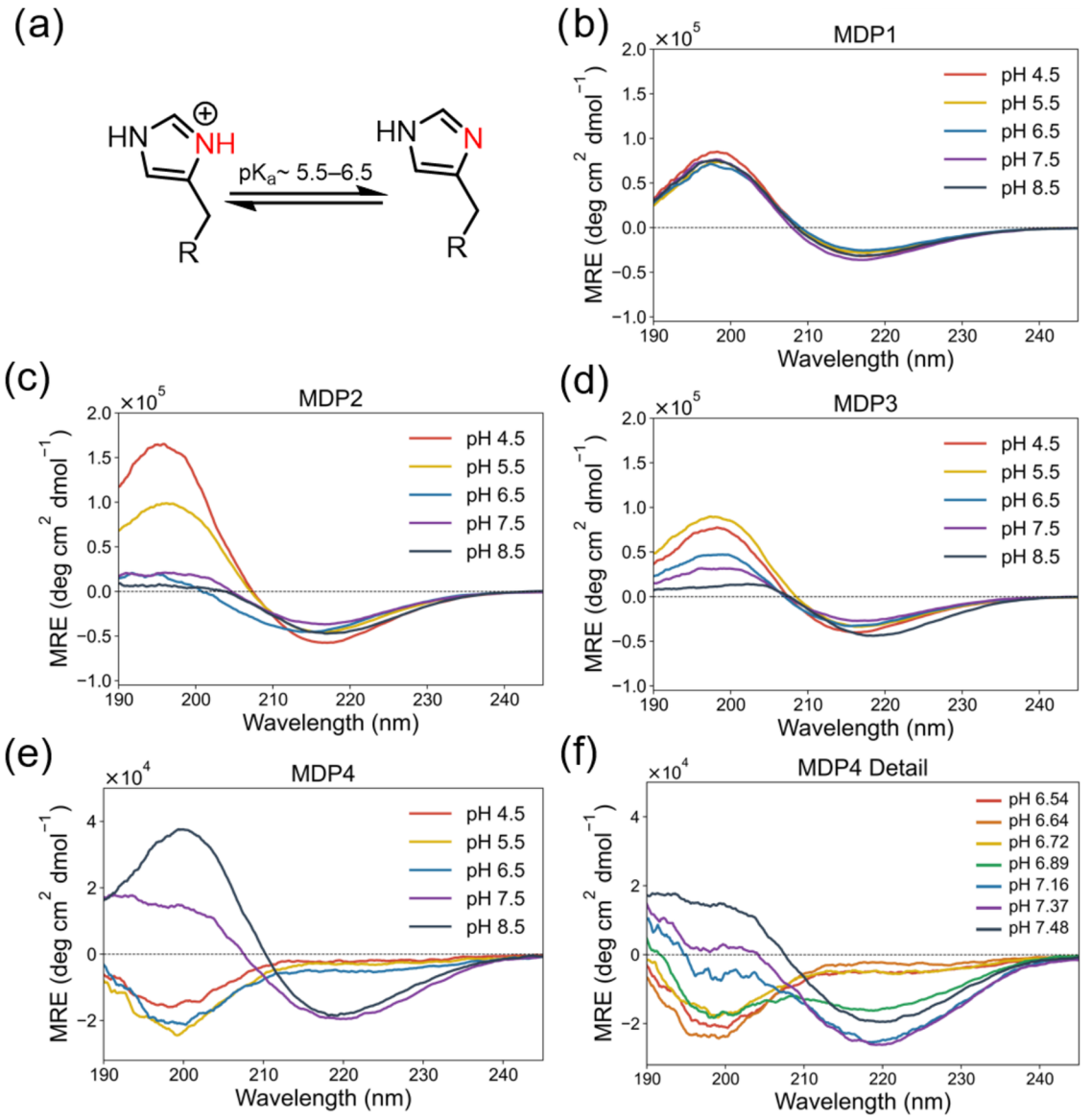

Figure 2. (a) Protonated and deprotonated forms of the imidazole side chain of histidine. CD spectra of peptides (b) MDP1, (c) MDP2, (d) MDP3, and (e) MDP4 across pHs 4.5−8.5 as well as (f) MPD4 across pH 6.5−7.5. MDP1−3 maintain a characteristic β-sheet of 198 nm maximum and 216 nm minimum across all pHs. MDP4 demonstrates a characteristic random coil 195 nm minimum and 215 nm maximum at pHs 6.7 and below before increasing in β-sheet formation with increasing pH, and fully adopting a β-sheet structure at pHs 7.5 and above.

plunge freezer (Leica Microsystems). The plunging chamber was set to have the following conditions: a temperature of 20 °C and a humidity of 90%. After preparation, samples were examined at the National Center for High-Resolution Electron Microscopy within Lund University on a JEM-2200FS (JEOL, Tokyo, Japan) transmission electron microscopy instrument using an F416.0 camera (TVIPS, Gauting, Germany) with an accelerator voltage of 200 kV. Zero-loss images were acquired using Serial EM in low-dose mode.

X-ray Scattering. Small-angle X-ray scattering (SAXS) measurements were performed at the CoSAXS beamline, MAX IV, Sweden. Experiments were performed using X-rays of wavelength of 0.69 Å (18 keV) and two sample-to-detector distances of 3.5 and 0.5 m. The two-dimensional X-ray detection was achieved using an Eiger2 4M detector. Samples were filled in a 1.5 mm quartz capillary using a robotic autoloader setup. Gels were diluted to 4 mg/mL to reduce the viscosity for SAXS measurements. Absolute intensity scattering data were processed using Python 3 (Figures S6−S9). Scattering data were modeled using SASview (https://www.sasview.org).

Equilibrium *In Vitro* Release Assay. Antimouse PD-1 antibody (BioXCell, Lebanon, NH) was labeled with tetrafluorophenyl (TFP) ester-functionalized AZDye 647 (Click Chemistry Tools, Scottsdale, AZ) using the protocol provided by the supplier to achieve a degree of labeling of 0.6 fluorophores per antibody. Labeled antibodies were prepared at 2 mg/mL in 2× PBS and hydrogels were prepared with this solution as previously described and corrected to pH 7.0 (±0.2). The release assay was run using a custom 3D-printed 48-well plate as previously reported.[57] 50 μL of each gel was plated into the depression on the left side of the elongated well before adding 1× PBS supernatant to fill the well (0.95 mL). PBS was pH corrected to 7.5 prior to addition using microliter scale additions of 1 M NaOH and HCl as needed. This same procedure was replicated for solutions mimicking 100% release by replicating peptide gel preparation and plating without the addition of peptide, as well as pipet mixing the solution and supernatant before starting the readings. The assay was immediately placed in a microplate reader (Tecan, Männedorf, Switzerland) following the addition of the supernatant. Time points were taken every 30 min for 24 h at 37 °C with 142 rpm orbital shaking by reading the fluorescence on the right side of each well where only supernatant would be present. Each run was then fitted to the two-phase kinetics model $C(t) = A_1(1 - e_1^{-kt}) + A_2(1 - e_2^{-kt})$,

https://doi.org/10.1021/acs.biomac.4c01296
Biomacromolecules 2025, 26, 490−502

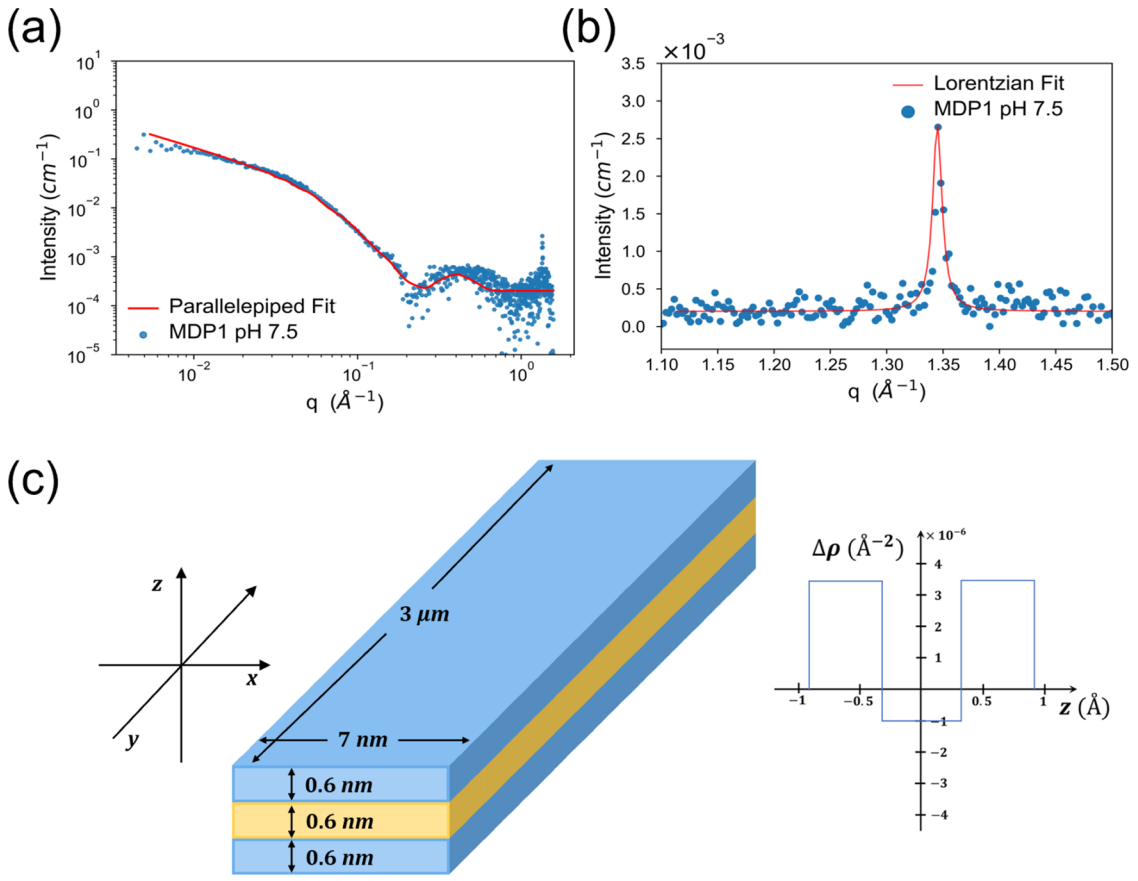

Figure 3. (a) Scattering peak at q = 1.3 $Å^{-1}$ of MDP1 fit with a Lorentzian equation with a relative width $\frac{\Delta q}{q}$ = 0.015. (b) SAXS curve of MDP1 at pH 7.5 overlaid with the core−shell parallelepiped model fit. (c) Illustration of the core−shell parallelepiped model for MDP1 at pH 7.5 with a hydrophobic core (yellow) and hydrophilic shell (blue). Shown on the right is the variation in the difference between the peptide and buffer scattering length density (SLD) across the z-axis, where the hydrophobic core has $\rho_c = 8 \times 10^{-6}$ $Å^{-2}$ and the hydrophilic shell has $\rho_s = 13 \times 10^{-6}$ $Å^{-2}$. Buffer SLD is equal to $\rho_b = 9.5 \times 10^{-6}$ $Å^{-2}$.

where $C(t)$ is the percent released at time t, A_1 is the amplitude of the first phase, k_1 is the rate constant of the first phase, A_2 is the amplitude of the second phase, and k_2 is the rate constant of the second phase.

Fluorescence Recovery after Photobleaching (FRAP). Hydrogels were prepared and loaded with labeled antibodies as previously described before being corrected to pH 6.5 and 7.5 (±0.05). Hydrogel aliquots (10 μL) were pipetted onto a 25 × 75 × 1 mm^3 Diamond White glass microscope slide (Globe Scientific Inc., Mahwah, NJ) in the center of a secure seal imaging spacer (Electron Microscopy Sciences, Hatfield, PA) and then covered with a 24 × 40 mm^2 cover glass (Corning Inc., Corning, NY). All FRAP experiments were conducted on a Nikon A1 Confocal microscope (Nikon, Tokyo, Japan) utilizing the NIS-Elements AR 5.21.03 software Galvano mode with a 20× objective lens, 512 × 512 pixel images, and a 50-pixel bleach spot diameter at a scan speed of 1 frame/s. Bleaching was performed by using 400, 486, 561, and 640 nm lasers at 100% intensity for 15.16 s to achieve a 90% bleach depth. The recovery in the fluorescent signal at the bleach site was monitored over 10 min using the 640 nm laser. Three different bleach spots were measured and recorded for each sample. Readings were corrected for background by subtracting the 10 s average before bleaching. To determine percent recovery, the fluorescence intensity of each gel was also divided by the initial reading prebleaching. The average of the three runs was plotted and fitted to $F_i(t) = A \times (1 - e^{-\tau \times t})$, where $F_i(t)$ is the corrected fluorescence recovery, A is the plateau intensity, and τ is the disassociation parameter. This can then be used to find the time to half recovery using $t_{1/2} = \ln 0.5/-\tau$.[58]

MTT Cytocompatibility Assay. Hydrogel aliquots (50 μL) were plated in a 48-well plate followed by the addition of a cell solution containing 30,000 3T3 fibroblasts (30 μL) and fresh 3T3 media (70 μL). At the 24 h time point, 100 μL of media was removed from each well and replaced with 100 μL of fresh media, along with 10 μL of MTT solution (3-(4,5-dimethylthiazol-2-yl)-2,5-diphenyltetrazolium bromide). The samples were incubated at 37 °C for 2 h. After incubation, the full volume was removed from each well, and 150 μL of DMSO was added to solubilize the resulting formazan crystals. Samples were pipet mixed as needed and further incubated at 37 °C for 15 min. Absorbance was then measured using a microplate reader (Tecan, Männedorf, Switzerland) at 560 nm. The protocol was repeated without the addition of the cell solution to create gel-only control samples and again without the addition of hydrogel to create cell-only control samples. Each sample was tested six times. Background values were subtracted from each absorbance measurement.

RESULTS AND DISCUSSION

Secondary Structure. Peptides were prepared by a standard solid-phase synthesis with N-terminal acetylation and C-terminal amidation. Crude peptide was purified by HPLC and subsequently confirmed by mass spectrometry. Peptide hydrogels were prepared by dissolving the peptide in MQ water at a concentration of 20 mg/mL and then adding an equal volume of 2× PBS to create a final 10 mg/mL (1 w/v%) solution. Each MDP hydrogel was prepared at a range of pH including 4.5, 5.5, 6.5, 7.5, and 8.5 to create a distribution of representative samples above and below histidine's pK_a while

https://doi.org/10.1021/acs.biomac.4c01296
Biomacromolecules 2025, 26, 490−502

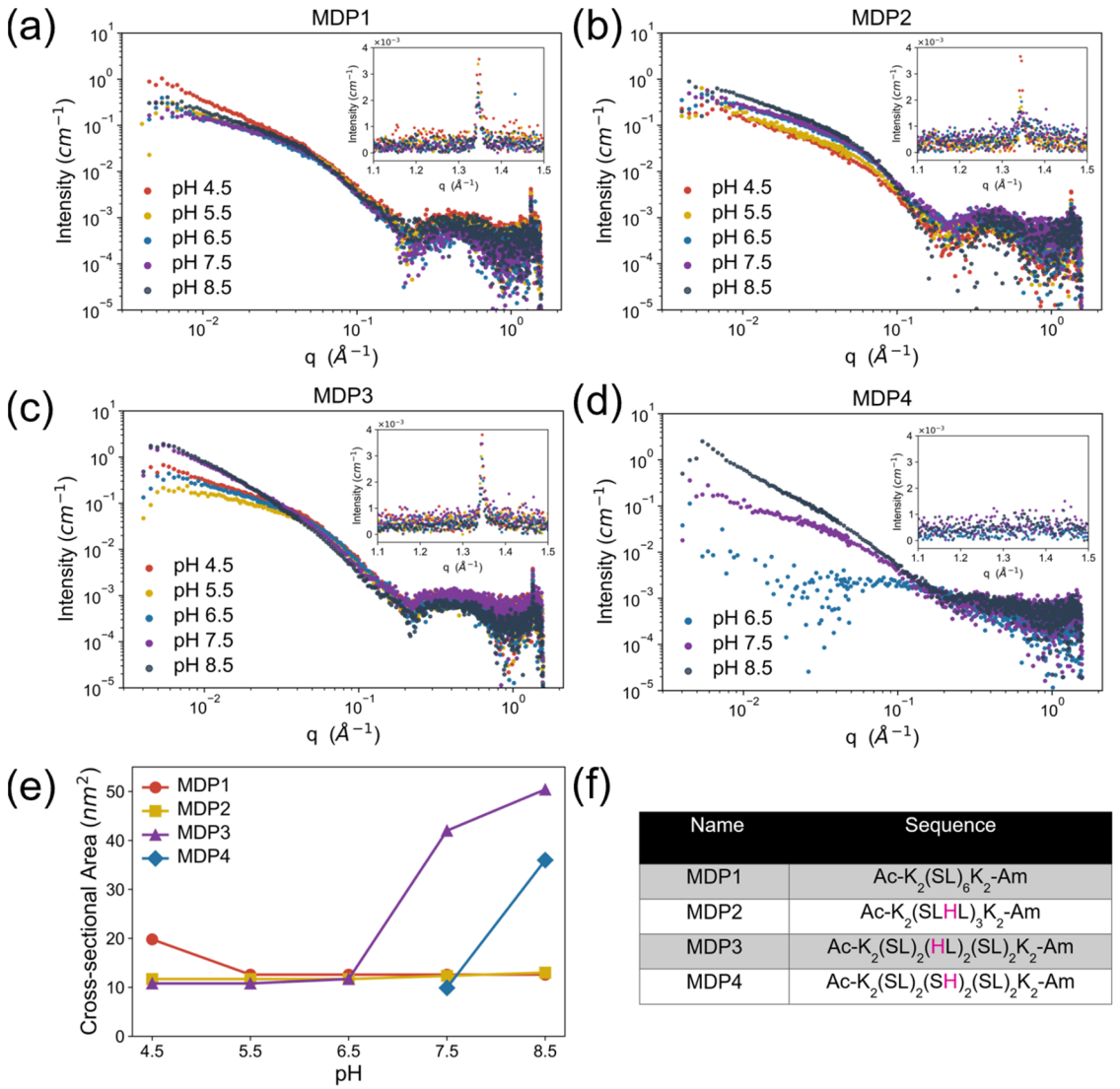

Name	Sequence
MDP1	Ac-$K_2(SL)_6K_2$-Am
MDP2	Ac-$K_2(SLHL)_3K_2$-Am
MDP3	Ac-$K_2(SL)_2(HL)_2(SL)_2K_2$-Am
MDP4	Ac-$K_2(SL)_2(SH)_2(SL)_2K_2$-Am

Figure 4. SAXS curves of (a) MDP1, (b) MDP2, (c) MDP3, and (d) MDP4 at pHs 4.5−8.5. Graph insets show a zoomed-in view of the scattering feature at 1.3 $Å^{-1}$. (e) Model extrapolated fiber cross-sectional areas for all hydrogels at pHs 4.5−8.5. Samples that did not assemble into nanofibers were omitted. (f) Sequence and naming conventions of MDP peptides with histidine substitutions highlighted in pink.

avoiding significant changes in the ionization state of other residues present (Figure 2a). The secondary structure of each peptide sequence over this pH range was examined by circular dichroism (CD) spectroscopy (Figure 2b−e). As previously reported, MDP1 adopted a typical β-sheet conformation with a maximum near 198 nm and a minimum near 216 nm with minimal variations across the entire pH range (Figure 2b).[45] The secondary structure of MDP1 was expected to not vary with pH over this range as the only ionizable amino acid residue it contains is lysine, which has a pK_a around 10.5 and the charge state is therefore expected to remain largely unaffected at and below pH 8.5.[59] Histidine substitutions in the hydrophilic face, as in MDP2 and MDP3, generally resulted in the same characteristic β-sheet conformation maxima and minima with notable decreases in mean residue ellipticity (MRE) intensity around the 198 nm peak as the pH increased (Figure 2c,d). When histidine was incorporated into the hydrophobic face, as in MDP4, there was a distinct shift in secondary structure with increasing pH (Figure 2e). Substituting the central hydrophobic leucine residues into MDP4 introduced a hydrophilic, protonatable residue that prevents the aggregation of the central B domain at pHs below the pK_a of histidine, as demonstrated by the minima at 195 nm characteristic to random coil confirmations at pHs 4.5−6.5. As the pH exceeds the pK_a of histidine at pH 7.5−8.5 and a higher fraction of histidine residues are in their neutral state (Figure 2a), there is a defined switch in secondary structure assembly as the hydrophilicity of the hydrophobic face decreases and the sequestering of the central domain becomes entropically favorable. A detailed CD analysis of MDP4 between pH 6.5 and 7.5 was performed to pinpoint this transition in the secondary structure (Figure 2f). At pHs 6.5−6.72, MDP4 maintained a random coil conformation with decreasing intensity before adopting characteristic CD features of both a random coil and β-sheet conformation at pHs 6.8−6.89 with a defined 195 nm minima consistent with random coil and 219 nm minima suggesting the presence of β-sheet. MDP4 appears to retain a mix of both conformations at pH 7.16 with an increasing 219 nm β-sheet minima until pH 7.48 where the random coil signal is no longer clearly observed.

Nanofiber Morphology. To determine how these observed pH-dependent changes in secondary structure

https://doi.org/10.1021/acs.biomac.4c01296
Biomacromolecules 2025, 26, 490−502

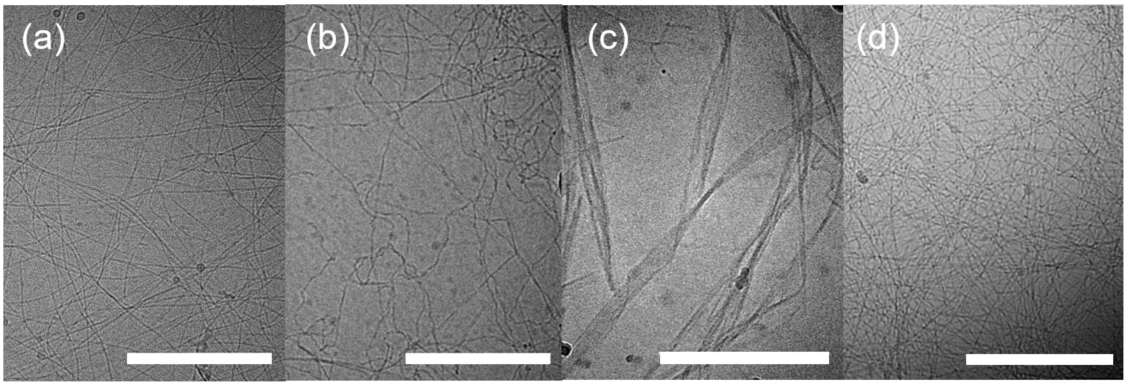

Figure 5. Cryo-TEM images of (a) MDP1, (b) MDP2, (c) MDP3, and (d) MDP4 at pHs 7.5. White scale bar represents 250 nm across all images. Dark circular spots in some images are residual ethane from cryogenic freezing.

influenced MDP higher-order assembly, the fiber morphology of each MDP was investigated by small-angle X-ray scattering to make high-resolution, Å-to-nm scale measurements of each peptide assembly. The scattering curve of MDP1 at pH 7.5 showed two prominent features in the high-q regime. The sharp peak near q = 1.3 Å^{-1} corresponds to a characteristic periodic β-strand separation of 4.7 Å.[60,61] Fitting this peak with a Lorentzian equation revealed that this reflection is very sharp and narrow, indicating that the β-sheets in MDP1 are well-ordered within the nanofibers (Figure 3a). The scattering curve also contained a broad reflection at around q = 0.5 Å^{-1} that is often observed in bilayer structures where the electron density is heterogeneous through the cross section of the scattering object (Figure 3b).[62] This feature is consistent with the prevailing model for MDP assembly where peptides form a "hydrophobic sandwich" that would appear as a bilayer-like scattering object (Figure 1). We found that the scattering curve of MDP1 at pH 7.5 could be accurately modeled as a 3-μm-long rigid parallelepiped with a 0.6 nm hydrophobic core flanked by two 0.6 nm hydrophilic layers (Figure 3c). The 1.8 nm fiber height used in this model is in good agreement with the uniform 2 nm measurement previously demonstrated by AFM height analysis. Extracting total fiber dimensions from this parallelepiped model also resulted in diameters consistent with the 6 ± 1 nm measurements previously found in Cryo-TEM images of MDP fibers.[45] These data provide the most conclusive support to date for the "hydrophobic sandwich" assembly model for MDPs and offer, for the first time, an estimate of the size of the hydrophobic core within the nanofibers.

MDP1, MDP2, and MDP3 SAXS curves agreed well with the previously described core−shell parallelepiped model across a pH range of 4.5−8.5 with minor deviations in the thicknesses of the core and shell layers. These models were subsequently used to calculate the average fiber dimensions of each sample as a function of pH (Figures S6−S9 and Tables S1 and S2). The scattering curves of MDP1 at pH 4.5−8.5 show little variation in both the low- and high-q regimes (Figure 4a). They all also exhibit nearly identical broad maxima around q = 0.5 Å^{-1} and a sharp peak near q = 1.3 Å^{-1}, indicating that MDP1 maintains a consistent bilayer-like and crystalline β-sheet structure. The dimensions of MDP1 fibers also remained constant across pH 5.5−8.5 and had a consistent cross-sectional area of 12.6 nm^2 (Figure 4e). Notably, a deviation in dimensions was noted in MDP1 at pH 4.5, which has the steepest low-q slope, as the fiber cross-sectional area increased marginally to 19.8 nm^2.

MDP2 and MDP3, which were designed to be pH-responsive, resulted in different pH-sensitive assemblies depending on the placement of the histidine residues in the MDP sequence. Both MDP2 and MDP3 fibers possessed the same β-sheet peak and bilayer-like scattering feature across all pHs, suggesting a consistent peptide packing in the fibers (Figure 4b,c). MDP2 maintained a cross-sectional area similar to MDP1 across all pHs with 11.57 nm^2 below pH 7.5 at which point it modestly increased to 12.35 nm^2 and increased again to 13.0 nm^2 at pH 8.5. The slope of scattering curves of MDP3 changed in the low-q regime (q = 0.006.0−0.01 Å^{-1}) across the different pH values, which reports on fiber clustering and aggregation. Rigid noninteracting fibers are expected to have a low-q slope of q^{-1}. A steeper slope suggests attractive fiber interactions, while a shallower slope suggests the presence of repulsive interactions. MDP3 fibers have a steady increase in slope within the low-q regime at higher pH, suggesting an increase in fibril aggregation at higher pHs. The fiber cross-sectional area of MDP3 demonstrated a trend similar to that with increasing pH. MDP3 fibers at pH 4.5 and 5.5 were smaller than MDP1 and MDP2 with a cross-sectional area of 10.8 nm^2 and had a small increase at pH 6.5 to 11.7 nm^2. At pH 7.5, the cross-sectional area of MDP3 dramatically increased by over 3-fold to 42.0 nm^2 and increased again at pH 8.5 to 50.4 nm^2, resulting in fibers over 4 times the cross-sectional area of canonical MDP1 fibers (Figure 4e).

Unlike the other sequences, MDP4 at pH 6.5 exhibited a noisy and mostly flat scattering curve characteristic of unstructured peptide without a uniform higher-order assembly (Figures 4d and S9).[63] This observation is consistent with the wide-angle X-ray scattering (WAXS) data for MDP4 at pHs 4.5 and 6.5 which all demonstrated broad curves indicative of undefined structures (Figure S10). These findings agree with the CD data that showed that MDP4 does not self-assemble at pH values below 6.8. At pH 7.5 and 8.5 SAXS revealed that MDP4 did form fibers but lacked the scattering features consistent with ordered β-sheet or laminated fibers and agreed best with a parallelepiped scattering model without a core. CD data indicate that MDP4 does self-assemble at pH 7.5 and 8.5, but the magnitude of the CD signal for MDP4 at both pHs is significantly lower MRE than that of the other MDP sequences (Figure 2). Since SAXS reflections arise from periodic structures in the sample, the absence of the scattering features observed in the other sequences suggests that the introduction

https://doi.org/10.1021/acs.biomac.4c01296
Biomacromolecules 2025, 26, 490−502

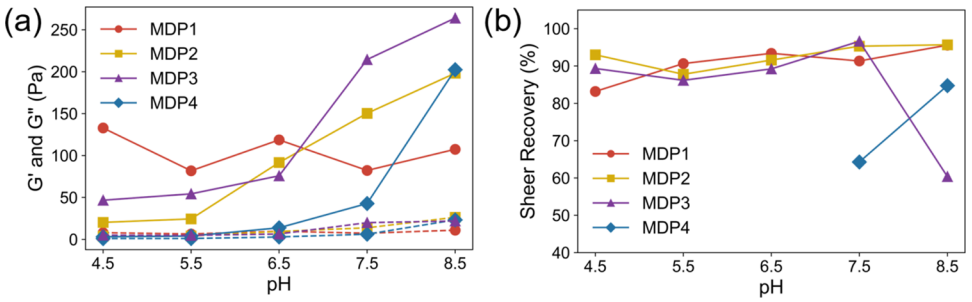

Figure 6. Rheological characterization of MDPs at pH 4.5−8.5. (a) Average G' (solid lines) and G'' (dashed lines) of each hydrogel after 30 min at a constant 1% strain. (b) Shear recovery of each hydrogel at varying pH as measured 10 min after shearing event. Samples without demonstrated gel formation were neglected in shear recovery analysis.

of histidine into an otherwise tightly packed hydrophobic core leads to increased heterogeneity in the fiber nanostructure even above the pK_a of histidine (Table S3). Like MDP3, the cross-sectional area of MDP4 increases at higher pH, which grows by over 3.5-fold from 9.5 nm^2 at pH 7.5 (smaller than that of MDP1 at that pH) to 36 nm^2 at pH 8.5 (Figure 4e). Although a small increase in cross-sectional area was similarly noted at low pH in MDP1, MDP3 and MDP4 both demonstrate larger changes in nanofiber dimensions at basic pH.

These trends in fiber formation were further studied by cryo-TEM (Figure 5a−d). In agreement with the SAXS observations that found MDP1 and MDP4 comparable low-q slopes and cross-sectional areas at pH 7.5, both peptides formed a homogeneous mixture of linear and unbranched nanofibers (Figure 5a,d). MDP2 at pH 7.5 formed a significantly less uniform network of curled, nonlinear fibers (Figure 5b) while MDP3 was observed to form a mixture of thicker, extended structures resembling nanotapes (Figures 5c and S11a). Consistent with the scattering data, the thicker nanofibers can be similarly observed in MDP4 at pH 8.5, although to a smaller degree than that seen in MDP3 (Figure S11b). The presence of these structures is likely responsible for the dramatic increase observed in the cross-sectional area as a function of increasing pH observed in SAXS. We initially hypothesized that the introduction of electrostatic repulsion at lower pH would prevent the uniform formation of fibers in MDP2 and MDP3 through the accumulation of charge along the fiber axis and increase fibril disorder. However, MDP2 and MDP3 at pH 4.5 form uniform elongated and high persistence length fibers comparable to MDP1 which agrees with the similar SAXS forms observed in all three gels (Figure S11c,d).

The difference in morphology between MDP2 and MDP3 suggests that the proximity and number of histidine residues within the peptide influence the nanofiber assembly. The central and consolidated locations of the two histidine substitutions in MDP3 appear to facilitate the emergence of stiff nanotape assemblies composed of multiple individual fibrils at high pH. The decrease in net charge with increasing pH allows for attractive interactions between neutral histidine residues to facilitate fiber aggregation, leading to an increase in the cross-sectional area. Increasing the distance between and the number of histidine residues in MDP2 results in curly low persistence length fibers at high pH. This phenomenon may be caused by the electrostatic repulsion between histidine residues, giving way to more attractive interactions at neutral to basic pH that enable the peptides, and thus fibers, to bend more readily.

Rheological Properties. To quantify the effects of these differing assemblies on the mechanical properties of each peptide hydrogel, oscillatory rheology experiments were performed over a pH range of 4.5−8.5 (Figure 6). MDP1, MDP2, and MDP3 maintained storage moduli (G') values larger than their respective loss moduli (G'') across all pHs, suggesting that they remain viscoelastic solids at the conditions tested (Figure 6a). MDP4 demonstrated no viscoelastic behavior at pHs 4.5, 5.5, and 6.5 with G' near 0 Pa and almost equal to G'' but began to exhibit G' values greater than G'' at pH 7.5 and pH 8.5 which aligns well with observed changes in secondary structure. MDP1 demonstrated a G' of approximately 100 Pa across all pH points, which is in agreement with previous investigations that successfully utilized MDP1 to control the release of encapsulated payloads *in vivo*.[50,64] Additionally, the rheological properties of MDP1 are comparable to RADA16 hydrogels, which are FDA-approved peptide-based hydrogels currently used in the clinic.[65,66] All three histidine-modified peptides demonstrated increases in G' as the pH increased, resulting in G' values larger than MDP1 at pH 8.5. MDP2 created a weak gel at low pHs but resulted in gels with a G' of 92 Pa, comparable to MDP1, at pH 6.5 and gels with a G' twice that of MDP1 at pH 8.5. MDP3 hydrogel strength also increased at higher pH. The G' of MDP3 nearly tripled from 76 to 215 Pa between pH 6.5 and 7.5 and resulted in a gel with a G' value near 264 Pa at pH 8.5, over double that of MDP1. MDP4 did not behave as a viscoelastic solid at pHs 4.5−6.5 with G' near 0 Pa and almost equal to G'' but began to exhibit G' values greater than G'' above pH 7.5. At pH 8.5, MDP4 had a significant increase in G' resulting in a gel near 200 Pa.

Although the introduction of electrostatic repulsion in the hydrophilic face did not eliminate fiber long-range assembly, we hypothesize that it perturbed intrafibrillar attractive interactions, resulting in MDP2 and MDP3 having similar fiber structures but with overall weakened gel networks compared to MDP1 at pH pHs 4.5−6.5. Previous work on MDP sequence variations has also found that varying the hydrophilic residues in the central domain influenced the hydrogen bonding quality between residues and thus the cohesive energy between peptides.[46] The increase in gel strength at high pH observed in MDPs with histidine substitutions may thus be the consequence of a new favorable hydrogen bonding network between histidine residues or between histidine and serine residues. Being that fiber diameter is also known to influence the mechanical properties of hydrogels, the observed increases in the cross-sectional area

https://doi.org/10.1021/acs.biomac.4c01296
Biomacromolecules 2025, 26, 490−502

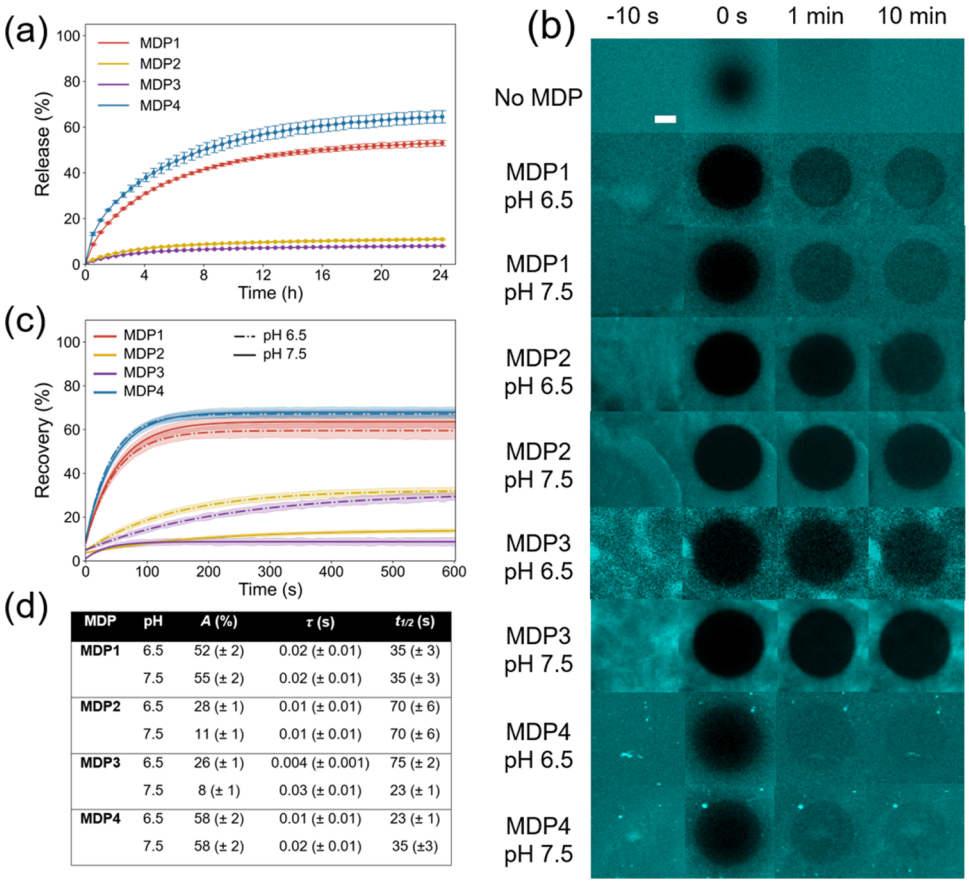

MDP	pH	A (%)	τ (s)	$t_{1/2}$ (s)
MDP1	6.5	52 (± 2)	0.02 (± 0.01)	35 (± 3)
	7.5	55 (± 2)	0.02 (± 0.01)	35 (± 3)
MDP2	6.5	28 (± 1)	0.01 (± 0.01)	70 (± 6)
	7.5	11 (± 1)	0.01 (± 0.01)	70 (± 6)
MDP3	6.5	26 (± 1)	0.004 (± 0.001)	75 (± 2)
	7.5	8 (± 1)	0.03 (± 0.01)	23 (± 1)
MDP4	6.5	58 (± 2)	0.01 (± 0.01)	23 (± 1)
	7.5	58 (± 2)	0.02 (± 0.01)	35 (±3)

Figure 7. (a) *In vitro* 24 h equilibrium release kinetics of MDP1−4 loaded with fluorescently labeled anti-PD-1 at pH 7.5 where dots are measured data and solid lines are fitted kinetic equations. (b) Images of MDP1−4 loaded with fluorescent anti-PD-1 before photobleaching (−10 s), immediately after bleaching (0 s), then 1 and 10 min after bleaching. White scale bar in the top left represents 20 μm. (c) Fitted FRAP kinetic curves of MDP1−4 loaded with fluorescent anti-PD-1 at pH 6.5 (dashed line) and 7.5 (solid line). Shaded areas indicate ± 1 standard deviation of experimental data. (d) Derived FRAP diffusion constants where A is the total fractional recovery, τ is the recovery time constant, and $t_{1/2}$ is the time until the sample reaches half of full recovery.

seen in MDP3 and MDP4 may also be driving the demonstrated increases in hydrogel strength at higher pHs.[67]

Supramolecular peptide hydrogels have the unique ability to recover their viscoelastic behavior after high deformation forces. This property is critical for injectable hydrogels used in biomedical applications, as the gel needs to reform after experiencing high shear forces while passing through a syringe needle. Thus, the shear recovery of the four peptide sequences was measured by monitoring the recovery of G' over 10 min after being subjected to 200% strain for 1 min (Figure 6b). Each MDP hydrogel demonstrated $G' < G''$ during the shearing event, suggesting that they behave as liquid under high deformation force and can thus be easily injected through a syringe for potential biomedical application (Figure S5). Regardless of their varying moduli, MDP1, MDP2, and MDP3 between pH 4.5 and 7.5 maintained high self-healing properties and recovered nearly 90% of their initial G'. MDP3 at pH 8.5, however, had a lower recovery, despite having the highest storage modulus of all MDP samples. We hypothesize that the slower recovery observed in MDP3 is due to the aggregate formation at this pH in response to high shear forces. SAXS and cryo-TEM data reveal that MDP3 fibers show a greater tendency to aggregate at high pH as deprotonation of lysine residues reduces the electrostatic repulsion between fibers. Aggregate formation upon shearing would limit the number of nanofibers available to participate in the hydrogel network and ultimately perturb shear recovery. MDP4 at pH 7.5 demonstrated a low shear recovery, around 64%, at pH 7.5 after 10 min but exhibited a higher recovery (85%) at pH 8.5. This increase in shear recovery is likely due to the reduced perturbation of the hydrophobic face of the MDP at high pH, which drives self-assembly.

Antibody Release Kinetics. Although MDP hydrogels have been previously used for the sustained release of a wide variety of bioactive compounds, the release rate of each molecule is heavily dependent on their peptide sequence, nanofiber morphology, hydrogel rheological properties, and the nature of the payload.[48,50] We thus hypothesized that the observed changes in the morphology and mechanical strength upon histidine modification would affect the controlled release properties from each hydrogel. To elucidate the controlled release capabilities of the histidine-functionalized peptides, we performed *in vitro* release assays using an anti-PD-1 antibody (anti-PD-1), FDA-approved immune checkpoint inhibitor for cancer immunotherapy, which has successfully been loaded into various peptide hydrogels, including MDP1, for use in preclinical cancer models.[64,68−71] Each peptide hydrogel was loaded with fluorescently conjugated anti-PD-1, submerged in pH 7.5 PBS, and the release of the antibody was measured using a fluorescence-based *in vitro* equilibrium release assay (Figure 7a). This assay reports on the equilibrium between the release of the payload from the hydrogel into the supernatant

https://doi.org/10.1021/acs.biomac.4c01296
Biomacromolecules 2025, 26, 490−502

and its retention and reabsorption in the hydrogel. Since this assay does not involve media replacement, these equilibrium release experiments serve to report on each hydrogel's propensity to retain encapsulated material, and the release profile reaches a plateau when the concentration outside the hydrogel is high enough such that the rate of release equals the rate of antibody diffusion back into the hydrorgel. Lower equilibrium release values, alongside slower rates of payload release, suggest that the payload has a higher affinity for the gel, whereas higher release rates closer to 100% suggest that the payload has less affinity to the hydrogel. Supramolecular peptide hydrogels typically have a two-phase release profile with a period of faster "burst" release followed by a slower second phase as the sample approaches equilibrium.[72] Release data were thus fitted to a biphasic model as detailed in the Experimental Methods section for ease of comparison (Table S4). Anti-PD-1 release from all peptides reached equilibrium at pH 7.5 within the 24 h time interval as observed by the flattening of the release curve at later time points. MDP4 had the highest initial burst and long-term release rate of all four peptides with a 24 h equilibrium release of 64.0 ± 1.2%, followed by MDP1 with a lower release of 53.0 ± 0.2%. By the end of the 24 h assay, both peptides with histidine in the hydrophilic face, MDP2 and MDP3, had significantly lower equilibrium releases. Only 11.0 ± 0.3% of the total anti-PD-1 had been released from MDP2 and 8.0 ± 0.3% had been released from MDP3, a significant decrease from the release observed in unmodified MDP1.

This dramatic decrease in release could be attributed to the fact that MDP2 and MDP3 form marginally stronger hydrogels than MDP1 at pH 7.5 by reducing the payload diffusion within the nanofiber matrix. Thus, the payload diffusivity was determined by a 10 min fluorescence recovery after photobleaching (FRAP) analysis at pH 6.5, where all three hydrogels have a comparable G', as well as at pH 7.5 (Figure 7b–d). FRAP kinetics analysis reports on the diffusion of the payload in the hydrogel into the photobleached area. Lower fluorescent recovery would correlate to a higher affinity between the payload and the gel matrix and subsequently suggests slower release if used *in vivo*. The data were modeled with a first-order exponential equation to extrapolate diffusion kinetics information, as described in the Experimental Methods section. FRAP trends were in good agreement with the 24 h release assay wherein MDP4 had the fastest and largest fluorescence recovery with a total recovery around 58 ± 2 and 58 ± 2% for pH 6.5 and 7.5, respectively, and a time to half recovery ($t_{1/2}$) of 23 ± 1 and 35 ± 3 s, respectively. This is followed by MDP1 with a total recovery of around 52 ± 2% at pH 6.5 and 55 ± 2% at pH 7.5 with a $t_{1/2}$ of 35 ± 3 s at both pHs. Interestingly, both MDP1 and MDP4 had a statistically similar recovery profile at both pHs despite notable differences in mechanical strength at pH 7.5 and the inability of MDP4 to form a hydrogel at pH 6.5.

MDP2 and MDP3 saw considerably less fluorescence recovery than MDP1 at both pH 6.5 and 7.5 (Figure 7b,c), which suggests that gel strength is not the primary factor dictating payload diffusion and release. If hydrogel strength was the primary characteristic driving release, MDP2 and MDP3 would demonstrate similar fluorescence recovery kinetics to MDP1 at pH 6.5 as they all have comparable storage moduli. Instead, MDP2 and MDP3 had 28 ± 1 and 26 ± 1% total recovery, respectively, a reduction of almost half of the fluorescence recovery observed in MDP1. These data suggest that attractive interactions between histidine residues and the payload play a pivotal role in the prolonged retention of anti-PD-1 inside the hydrogel matrix. Interestingly, despite comparable gel strengths and one less histidine residue, MDP3, with 8 ± 1% total recovery at pH 7.5, demonstrated a slower release than MDP2, with a fluorescence recovery of 11 ± 1%. It can thus be concluded that not only the presence, but the spatial placement of histidine in the hydrogel matrix influences the retention of the antibody payload. Notably, supramolecular assembly plays a pivotal role in FRAP kinetics as MDP2 and MDP3 demonstrated pH-responsive fluorescence recovery behavior with a 60 and 70% decrease in recovery as pH increased from 6.5 to 7.5, respectively.

The attractive interactions between anti-PD-1 and these histidine-functionalized nanofibers that slow release from the hydrogel are likely the result of multiple synergistic noncovalent forces. Of all the canonical amino acids, histidine is uniquely suitable to able to interact with the widest diversity of other residues due to its versatile imidazole side-chain.[73] Histidine, in its neutral form, can interact with positively charged and polar residues through cation−π and hydrogen bonding interactions, respectively, and can simultaneously interact with nonpolar, aromatic residues through $\pi-\pi$ and hydrogen−π interactions. When positively charged, histidine can additionally form salt bridges with negatively charged residues When positively charged, histidine can additionally form salt bridges with negatively charged residues and introduce repulsive electrostatic interactions with other positively charged residues. These interactions would uniquely contribute to the varying release profiles of antibody payloads based on individual isoelectric points and surface charges.

Histidine is thus granted a nonspecific affinity for a wide range of protein surface moieties that can be strategically leveraged to modulate the release of various protein-based payloads. These histidine-functionalized MDPs exploit these versatile properties and show a significantly prolonged release compared with unmodified MDP1 through the simple substitution of amino acid residues. Given MDP3's slow-release profile, along with its favorable mechanical properties and pH-responsive self-assembly, we identified it as the most promising candidate for further investigation and performed an MTT assay to confirm its biocompatibility (Figure S12). Cells cultured with MDP1 and MDP3 exhibited significantly increased MTT metabolism compared to that of the cell-only control, suggesting enhanced cell proliferation. MDP1 and MDP3 also showed no statistically significant difference in MTT metabolism, highlighting MDP3's strong potential for biological applications and suggesting that histidine-modified MDPs are equally cytocompatible as unmodified MDPs. Thus, these novel MDPs are attractive future candidates for prolonged antibody drug delivery and expand the toolbox for the controlled release of therapeutic or prophylactic proteins from MDPs.

CONCLUSIONS

Herein, we have designed histidine-functionalized self-assembling MDPs that exhibit pH-responsive behavior, in accordance with the number and position of histidine substitutions. Histidine residues within the hydrophobic core of the MDP sequence create novel peptides that disassemble below the physiological pH and form nanofibers comparable to unmodified MDPs at higher pHs. Histidine substitutions in the hydrophilic peptide face result in similar morphologies and

https://doi.org/10.1021/acs.biomac.4c01296
Biomacromolecules 2025, 26, 490−502

weaker gels compared to unmodified MDPs at pHs below the pK_a of histidine but higher-order assemblies and stronger gels at pHs below or above 7.5. Our results also demonstrate that including histidine within the hydrophilic face of MDPs significantly reduces diffusivity in the hydrogel and delays the release of anti-PD-1 antibodies, further implicating MDPs as efficient drug delivery vehicles as well as demonstrating that favorable interactions between histidine and antibody surface residues can be leveraged for use in controlled release systems. In conjunction with their pH-responsive morphology and release, these properties make MDPs particularly promising for the controlled release of therapeutics in response to the acidic tumor microenvironment. This study shows how simple and rational variations in the MDP structure can yield robust stimulus-responsive hydrogels with unique properties.

■ ASSOCIATED CONTENT

Supporting Information

The Supporting Information is available free of charge at https://pubs.acs.org/doi/10.1021/acs.biomac.4c01296.

Mass and LC characterization of peptides, additional CD and rheology, SAXS model fitting, WAXS, cryo-TEM, release assay fitting, and cell viability assay (PDF)

■ AUTHOR INFORMATION

Corresponding Authors

Kevin J. McHugh − *Department of Chemistry, Rice University, Houston, Texas 77005, United States; Department of Bioengineering, Rice University, Houston, Texas 77005, United States;* orcid.org/0000-0001-6801-4431; Email: kevin.mchugh@rice.edu

Jeffrey D. Hartgerink − *Department of Chemistry, Rice University, Houston, Texas 77005, United States; Department of Bioengineering, Rice University, Houston, Texas 77005, United States;* orcid.org/0000-0002-3186-5395; Email: jdh@rice.edu

Authors

Gabriel Saenz − *Department of Chemistry, Rice University, Houston, Texas 77005, United States;* orcid.org/0000-0001-7124-7703

Brett H. Pogostin − *Department of Bioengineering, Rice University, Houston, Texas 77005, United States;* orcid.org/0000-0002-1462-4442

Carson C. Cole − *Department of Chemistry, Rice University, Houston, Texas 77005, United States;* orcid.org/0000-0002-7573-1882

Anushka Agrawal − *Department of Bioengineering, Rice University, Houston, Texas 77005, United States*

Danielle Chew-Martinez − *Department of Chemistry, Rice University, Houston, Texas 77005, United States*

Marija Dubackic − *Division of Physical Chemistry, Lund University, Lund SE-221 00, Sweden;* orcid.org/0000-0002-9037-828X

Antara Pal − *Department of Physics, Stockholm University, Stockholm SE-221 00, Sweden; MAX IV Laboratory, Lund SE-221 00, Sweden;* orcid.org/0000-0002-8998-6771

Ulf Olsson − *Division of Physical Chemistry, Lund University, Lund SE-221 00, Sweden;* orcid.org/0000-0003-2200-1605

Complete contact information is available at: https://pubs.acs.org/10.1021/acs.biomac.4c01296

Author Contributions

#G.S. and B.H.P. contributed equally.

Notes

The authors declare the following competing financial interest(s): KJM is a consultant for Nanocan Therapeutics and Omnipulse Biosciences whose work is unrelated to MDPs.

■ ACKNOWLEDGMENTS

The authors acknowledge Fátima Herranz for her assistance at the CoSAXS beamline at MAX IV, and Le Tracy Yu and Crispin Hetherington for their expertise with Cryo-TEM. This work was supported in part by grants from the Welch Foundation (C-2141) and the NIH (R01 DE021798 and R01 DE030140). This work was additionally supported by funding from the Swedish Research Council (Grant Number 2020-04633). B.H.P. and C.C.C. were supported by the NSF Graduate Student Research Fellowship (Grant Number 1842494). B.H.P. was supported by NCI F99/K00 Award No. F99CA284262. This work was done in part using resources of the Shared Equipment Authority at Rice University. This work benefited from the use of the SasView application, originally developed under NSF award DMR-0520547. SasView contains code developed with funding from the European Union's Horizon 2020 Research and Innovation Program under the SINE2020 project, Grant Agreement No. 654000. We acknowledge the MAX IV Laboratory for beamtime on the CoSAXS beamline under proposal 20220368. Research conducted at MAX IV, a Swedish national user facility, is supported by Vetenskapsrådet (Swedish Research Council, VR) under contract 2018-07152, Vinnova (Swedish Governmental Agency for Innovation Systems) under contract 2018-04969 and Formas under contract 2019-02496.

■ REFERENCES

(1) Worthington, P.; Pochan, D. J.; Langhans, S. A. Peptide Hydrogels − Versatile Matrices for 3D Cell Culture in Cancer Medicine. *Front. Oncol.* **2015**, *5*, No. 92, DOI: 10.3389/fonc.2015.00092.

(2) Sun, L.; Zheng, C.; Webster, T. J. Self-Assembled Peptide Nanomaterials for Biomedical Applications: Promises and Pitfalls. *Int. J. Nanomed.* **2017**, *12*, 73−86.

(3) Dvořáková, J.; Trousil, J.; Podhorská, B.; Mikšovská, Z.; Janoušková, O.; Proks, V. Enzymatically Cross-Linked Hydrogels Based on Synthetic Poly(α-Amino Acid)s Functionalized with RGD Peptide for 3D Mesenchymal Stem Cell Culture. *Biomacromolecules* **2021**, *22* (4), 1417−1431.

(4) Li, R.; Sun, Y.; Cai, Z.; Li, Y.; Sun, J.; Bi, W.; Yang, F.; Zhou, Q.; Ye, T.; Yu, Y. Highly Bioactive Peptide-HA Photo-Crosslinking Hydrogel for Sustained Promoting Bone Regeneration. *Chem. Eng. J.* **2021**, *415*, No. 129015.

(5) Kotko, O.; Šálek, P.; Dvořáková, J.; Smrčková, M. D.; Šomvársky, J.; Bonvent, J. J.; Brochsztain, S.; Šlouf, M.; Proks, V. Soft Micron-Sized Polypeptide Microgels: Preparation, Crosslink Density, Topography and Nanomechanics in Swollen State. *Mater. Adv.* **2024**, *5* (14), 5984−5997.

(6) Dong, Y.; Ramey-Ward, A. N.; Salaita, K. Programmable Mechanically Active Hydrogel-Based Materials. *Adv. Mater.* **2021**, *33* (46), No. 2006600.

(7) Duti, I. J.; Florian, J. R.; Kittel, A. R.; Amelung, C. D.; Gray, V. P.; Lampe, K. J.; Letteri, R. A. Peptide Stereocomplexation Orchestrates Supramolecular Assembly of Hydrogel Biomaterials. *J. Am. Chem. Soc.* **2023**, *145* (33), 18468−18476.

(8) Lian, M.; Chen, X.; Lu, Y.; Yang, W. Self-Assembled Peptide Hydrogel as a Smart Biointerface for Enzyme-Based Electrochemical

Biosensing and Cell Monitoring. *ACS Appl. Mater. Interfaces* **2016**, *8* (38), 25036−25042.
(9) Griffin, D. R.; Archang, M. M.; Kuan, C.-H.; Weaver, W. M.; Weinstein, J. S.; Feng, A. C.; Ruccia, A.; Sideris, E.; Ragkousis, V.; Koh, J.; Plikus, M. V.; Di Carlo, D.; Segura, T.; Scumpia, P. O. Activating an Adaptive Immune Response from a Hydrogel Scaffold Imparts Regenerative Wound Healing. *Nat. Mater.* **2021**, *20* (4), 560−569.
(10) Galler, K. M.; Hartgerink, J. D.; Cavender, A. C.; Schmalz, G.; D'Souza, R. N. A Customized Self-Assembling Peptide Hydrogel for Dental Pulp Tissue Engineering. *Tissue Eng., Part A* **2012**, *18* (1−2), 176−184.
(11) Koutsopoulos, S. Self-Assembling Peptide Nanofiber Hydrogels in Tissue Engineering and Regenerative Medicine: Progress, Design Guidelines, and Applications. *J. Biomed. Mater. Res., Part A* **2016**, *104* (4), 1002−1016.
(12) Jin, H.; Wan, C.; Zou, Z.; Zhao, G.; Zhang, L.; Geng, Y.; Chen, T.; Huang, A.; Jiang, F.; Feng, J.-P.; Lovell, J. F.; Chen, J.; Wu, G.; Yang, K. Tumor Ablation and Therapeutic Immunity Induction by an Injectable Peptide Hydrogel. *ACS Nano* **2018**, *12* (4), 3295−3310.
(13) Nagy-Smith, K.; Yamada, Y.; Schneider, J. P. Protein Release from Highly Charged Peptide Hydrogel Networks. *J. Mater. Chem. B* **2016**, *4* (11), 1999−2007.
(14) Yang, J.; Yao, M.-H.; Jin, R.-M.; Zhao, D.-H.; Zhao, Y.-D.; Liu, B. Polypeptide-Engineered Hydrogel Coated Gold Nanorods for Targeted Drug Delivery and Chemo-Photothermal Therapy. *ACS Biomater. Sci. Eng.* **2017**, *3* (10), 2391−2398.
(15) Feng, F.; Song, X.; Tan, Z.; Tu, Y.; Xiao, L.; Xie, P.; Ma, Y.; Sun, X.; Ma, J.; Rong, L.; He, L. Cooperative Assembly of a Designer Peptide and Silk Fibroin into Hybrid Nanofiber Gels for Neural Regeneration after Spinal Cord Injury. *Sci. Adv.* **2023**, *9* (25), No. eadg0234.
(16) Kaur, H.; Sharma, P.; Patel, N.; Pal, V. K.; Roy, S. Accessing Highly Tunable Nanostructured Hydrogels in a Short Ionic Complementary Peptide Sequence via pH Trigger. *Langmuir* **2020**, *36* (41), 12107−12120.
(17) Wang, L.; Gong, C.; Yuan, X.; Wei, G. Controlling the Self-Assembly of Biomolecules into Functional Nanomaterials through Internal Interactions and External Stimulations: A Review. *Nanomaterials* **2019**, *9* (2), 285.
(18) Ghosh, A.; Haverick, M.; Stump, K.; Yang, X.; Tweedle, M. F.; Goldberger, J. E. Fine-Tuning the pH Trigger of Self-Assembly. *J. Am. Chem. Soc.* **2012**, *134* (8), 3647−3650.
(19) Pramanik, B.; Ahmed, S. Peptide-Based Low Molecular Weight Photosensitive Supramolecular Gelators. *Gels* **2022**, *8* (9), 533.
(20) Pedersen, S. L.; Huynh, T. H.; Pöschko, P.; Fruergaard, A. S.; Jarlstad Olesen, M. T.; Chen, Y.; Birkedal, H.; Subbiahdoss, G.; Reimhult, E.; Thøgersen, J.; Zelikin, A. N. Remotely Triggered Liquefaction of Hydrogel Materials. *ACS Nano* **2020**, *14* (7), 9145−9155.
(21) Zhuo, S.; Zhang, F.; Yu, J.; Zhang, X.; Yang, G.; Liu, X. pH-Sensitive Biomaterials for Drug Delivery. *Molecules* **2020**, *25* (23), 5649.
(22) Liu, Y.; Zhang, D.; Qiao, Z.-Y.; Qi, G.-B.; Liang, X.-J.; Chen, X.-G.; Wang, H. A Peptide-Network Weaved Nanoplatform with Tumor Microenvironment Responsiveness and Deep Tissue Penetration Capability for Cancer Therapy. *Adv. Mater.* **2015**, *27* (34), 5034−5042.
(23) Raza, F.; Zhu, Y.; Chen, L.; You, X.; Zhang, J.; Khan, A.; Waseem Khan, M.; Hasnat, M.; Zafar, H.; Wu, J.; Ge, L. Paclitaxel-Loaded pH Responsive Hydrogel Based on Self-Assembled Peptides for Tumor Targeting. *Biomater. Sci.* **2019**, *7* (5), 2023−2036.
(24) Mei, L.; Xu, K.; Zhai, Z.; He, S.; Zhu, T.; Zhong, W. Doxorubicin-Reinforced Supramolecular Hydrogels of RGD-Derived Peptide Conjugates for pH-Responsive Drug Delivery. *Org. Biomol. Chem.* **2019**, *17* (15), 3853−3860.
(25) Zhu, J.; Gao, R.; Wang, Z.; Cheng, Z.; Xu, Z.; Liu, Z.; Wu, Y.; Wang, M.; Zhang, Y. Sustained and Targeted Delivery of Self-Assembled Doxorubicin Nonapeptides Using pH-Responsive Hydrogels for Osteosarcoma Chemotherapy. *Pharmaceutics* **2023**, *15* (2), 668.
(26) Huang, X.; Liao, W.; Xie, Z.; Chen, D.; Zhang, C. Y. A pH-Responsive Prodrug Delivery System Self-Assembled from Acid-Labile Doxorubicin-Conjugated Amphiphilic pH-Sensitive Block Copolymers. *Mater. Sci. Eng. C* **2018**, *90*, 27−37.
(27) Zhang, J.; Lin, W.; Yang, L.; Zhang, A.; Zhang, Y.; Liu, J.; Liu, J. Injectable and pH-Responsive Self-Assembled Peptide Hydrogel for Promoted Tumor Cell Uptake and Enhanced Cancer Chemotherapy. *Biomater. Sci.* **2022**, *10* (3), 854−862.
(28) Balcı, B.; Top, A. PEG and PEG-Peptide Based Doxorubicin Delivery Systems Containing Hydrazone Bond. *J. Polym. Res.* **2018**, *25* (4), 104.
(29) Li, Z.; Zhu, Y.; Matson, J. B. pH-Responsive Self-Assembling Peptide-Based Biomaterials: Designs and Applications. *ACS Appl. Bio Mater.* **2022**, *5* (10), 4635−4651.
(30) Pieszka, M.; Han, S.; Volkmann, C.; Graf, R.; Lieberwirth, I.; Landfester, K.; Ng, D. Y. W.; Weil, T. Controlled Supramolecular Assembly Inside Living Cells by Sequential Multistaged Chemical Reactions. *J. Am. Chem. Soc.* **2020**, *142* (37), 15780−15789.
(31) Zafar, S.; Beg, S.; Panda, S. K.; Rahman, M.; Alharbi, K. S.; Jain, G. K.; Ahmad, F. J. Novel Therapeutic Interventions in Cancer Treatment Using Protein and Peptide-Based Targeted Smart Systems. *Semin. Cancer Biol.* **2021**, *69*, 249−267.
(32) Bao, X.; Si, X.; Ding, X.; Duan, L.; Xiao, C. pH-Responsive Hydrogels Based on the Self-Assembly of Short Polypeptides for Controlled Release of Peptide and Protein Drugs. *J. Polym. Res.* **2019**, *26* (12), 278.
(33) Frohm, B.; E DeNizio, J.; M Lee, D. S.; Gentile, L.; Olsson, U.; Malm, J.; S Åkerfeldt, K.; Linse, S. A Peptide from Human Semenogelin I Self-Assembles into a pH-Responsive Hydrogel. *Soft Matter* **2015**, *11* (2), 414−421.
(34) Wang, P.; Liu, W.; Liu, S.; Yang, R.; Pu, Y.; Zhang, W.; Wang, X.; Liu, X.; Ren, Y.; Chi, B. pH-Responsive Nanomicelles of Poly(Ethylene Glycol)-Poly(ε-Caprolactone)-Poly(L-Histidine) for Targeted Drug Delivery. *J. Biomater. Sci., Polym. Ed.* **2020**, *31* (3), 277−292.
(35) Pogostin, B. H.; Malmendal, A.; Londergan, C. H.; Åkerfeldt, K. S. pKa Determination of a Histidine Residue in a Short Peptide Using Raman Spectroscopy. *Molecules* **2019**, *24* (3), 405.
(36) Valéry, C.; Deville-Foillard, S.; Lefebvre, C.; Taberner, N.; Legrand, P.; Meneau, F.; Meriadec, C.; Delvaux, C.; Bizien, T.; Kasotakis, E.; Lopez-Iglesias, C.; Gall, A.; Bressanelli, S.; Le Du, M.-H.; Paternostre, M.; Artzner, F. Atomic View of the Histidine Environment Stabilizing Higher-pH Conformations of pH-Dependent Proteins. *Nat. Commun.* **2015**, *6* (1), No. 7771.
(37) De Toma, A. S.; Salamekh, S.; Ramamoorthy, A.; Hee Lim, M. Misfolded Proteins in Alzheimer's Disease and Type II Diabetes. *Chem. Soc. Rev.* **2012**, *41* (2), 608−621.
(38) Hua, J.; Wang, F.; Wei, X.; Qin, Y.; Lian, J.; Wu, J.; Ma, P.; Ma, X. A Nanoenzyme Constructed from Manganese and Strandberg-Type Phosphomolybdate with Versatility in Antioxidant and Modulating Conformation of Aβ Protein Misfolding Aggregates In Vitro. *Int. J. Mol. Sci.* **2023**, *24* (5), 4317.
(39) Callahan, D. J.; Liu, W.; Li, X.; Dreher, M. R.; Hassouneh, W.; Kim, M.; Marszalek, P.; Chilkoti, A. Triple Stimulus-Responsive Polypeptide Nanoparticles That Enhance Intratumoral Spatial Distribution. *Nano Lett.* **2012**, *12* (4), 2165−2170.
(40) Zhang, L.; Xu, J.; Wang, F.; Ding, Y.; Wang, T.; Jin, G.; Martz, M.; Gui, Z.; Ouyang, P.; Chen, P. Histidine-Rich Cell-Penetrating Peptide for Cancer Drug Delivery and Its Uptake Mechanism. *Langmuir* **2019**, *35* (9), 3513−3523.
(41) Swietach, P.; Boedtkjer, E.; Pedersen, S. F. How Protons Pave the Way to Aggressive Cancers. *Nat. Rev. Cancer* **2023**, *23* (12), 825−841.
(42) Chang, G.; Li, C.; Lu, W.; Ding, J. N-Boc-Histidine-Capped PLGA-PEG-PLGA as a Smart Polymer for Drug Delivery Sensitive to Tumor Extracellular pH. *Macromol. Biosci.* **2010**, *10* (10), 1248−1256.

https://doi.org/10.1021/acs.biomac.4c01296
Biomacromolecules 2025, 26, 490−502

(43) Yin, H.; Lee, E. S.; Kim, D.; Lee, K. H.; Oh, K. T.; Bae, Y. H. Physicochemical Characteristics of pH-Sensitive Poly(l-Histidine)-b-Poly(Ethylene Glycol)/Poly(l-Lactide)-b-Poly(Ethylene Glycol) Mixed Micelles. *J. Controlled Release* **2008**, *126* (2), 130−138.
(44) Xie, L.; Liu, R.; Chen, X.; He, M.; Zhang, Y.; Chen, S. Micelles Based on Lysine, Histidine, or Arginine: Designing Structures for Enhanced Drug Delivery. *Front. Bioeng. Biotechnol.* **2021**, *9*, No. 744657, DOI: 10.3389/fbioe.2021.744657.
(45) Dong, H.; Paramonov, S. E.; Aulisa, L.; Bakota, E. L.; Hartgerink, J. D. Self-Assembly of Multidomain Peptides: Balancing Molecular Frustration Controls Conformation and Nanostructure. *J. Am. Chem. Soc.* **2007**, *129* (41), 12468−12472.
(46) Aulisa, L.; Dong, H.; Hartgerink, J. D. Self-Assembly of Multidomain Peptides: Sequence Variation Allows Control over Cross-Linking and Viscoelasticity. *Biomacromolecules* **2009**, *10* (9), 2694−2698.
(47) Bakota, E. L.; Sensoy, O.; Ozgur, B.; Sayar, M.; Hartgerink, J. D. Self-Assembling Multidomain Peptide Fibers with Aromatic Cores. *Biomacromolecules* **2013**, *14* (5), 1370−1378.
(48) Moore, A. N.; Hartgerink, J. D. Self-Assembling Multidomain Peptide Nanofibers for Delivery of Bioactive Molecules and Tissue Regeneration. *Acc. Chem. Res.* **2017**, *50* (4), 714−722.
(49) Lopez-Silva, T. L.; Cristobal, C. D.; Edwin Lai, C. S.; Leyva-Aranda, V.; Lee, H. K.; Hartgerink, J. D. Self-Assembling Multidomain Peptide Hydrogels Accelerate Peripheral Nerve Regeneration after Crush Injury. *Biomaterials* **2021**, *265*, No. 120401.
(50) Pogostin, B. H.; Yu, M. H.; Azares, A. R.; Euliano, E. M.; Lai, C. S. E.; Saenz, G.; Wu, S. X.; Farsheed, A. C.; Melhorn, S. M.; Graf, T. P.; Woodside, D. G.; Hartgerink, J. D.; McHugh, K. J. Multidomain Peptide Hydrogel Adjuvants Elicit Strong Bias towards Humoral Immunity. *Biomater. Sci.* **2022**, *10* (21), 6217−6229.
(51) Lopez-Silva, T. L.; Leach, D. G.; Azares, A.; Li, I.-C.; Woodside, D. G.; Hartgerink, J. D. Chemical Functionality of Multidomain Peptide Hydrogels Governs Early Host Immune Response. *Biomaterials* **2020**, *231*, No. 119667.
(52) Li, I.-C.; Moore, A. N.; Hartgerink, J. D. Missing Tooth" Multidomain Peptide Nanofibers for Delivery of Small Molecule Drugs. *Biomacromolecules* **2016**, *17* (6), 2087−2095.
(53) Carrejo, N. C.; Moore, A. N.; Lopez Silva, T. L.; Leach, D. G.; Li, I.-C.; Walker, D. R.; Hartgerink, J. D. Multidomain Peptide Hydrogel Accelerates Healing of Full-Thickness Wounds in Diabetic Mice. *ACS Biomater. Sci. Eng.* **2018**, *4* (4), 1386−1396.
(54) Kumar, V. A.; Taylor, N. L.; Shi, S.; Wickremasinghe, N. C.; D'Souza, R. N.; Hartgerink, J. D. Self-Assembling Multidomain Peptides Tailor Biological Responses through Biphasic Release. *Biomaterials* **2015**, *52*, 71−78.
(55) Wickremasinghe, N. C.; Kumar, V. A.; Hartgerink, J. D. Two-Step Self-Assembly of Liposome-Multidomain Peptide Nanofiber Hydrogel for Time-Controlled Release. *Biomacromolecules* **2014**, *15* (10), 3587−3595.
(56) Lopez-Silva, T. L.; Leach, D. G.; Li, I.-C.; Wang, X.; Hartgerink, J. D. Self-Assembling Multidomain Peptides: Design and Characterization of Neutral Peptide-Based Materials with pH and Ionic Strength Independent Self-Assembly. *ACS Biomater. Sci. Eng.* **2019**, *5* (2), 977−985.
(57) Pogostin, B. H.; Saenz, G.; Cole, C. C.; Euliano, E. M.; Hartgerink, J. D.; McHugh, K. J. Dynamic Imine Bonding Facilitates Mannan Release from a Nanofibrous Peptide Hydrogel. *Bioconjugate Chem.* **2023**, *34* (1), 193−203.
(58) Kang, M.; Day, C. A.; Kenworthy, A. K.; DiBenedetto, E. Simplified Equation to Extract Diffusion Coefficients from Confocal FRAP Data. *Traffic* **2012**, *13* (12), 1589−1600.
(59) Grimsley, G. R.; Scholtz, J. M.; Pace, C. N. A Summary of the Measured pK Values of the Ionizable Groups in Folded Proteins. *Protein Sci.* **2009**, *18* (1), 247−251.
(60) Serpell, L. C.; Berriman, J.; Jakes, R.; Goedert, M.; Crowther, R. A. Fiber Diffraction of Synthetic α-Synuclein Filaments Shows Amyloid-like Cross-β Conformation. *Proc. Natl. Acad. Sci. U.S.A.* **2000**, *97* (9), 4897−4902.
(61) Pogostin, B. H.; Linse, S.; Olsson, U. Fibril Charge Affects α-Synuclein Hydrogel Rheological Properties. *Langmuir* **2019**, *35* (50), 16536−16544.
(62) Dubackic, M.; Linse, S.; Sparr, E.; Olsson, U. Comparing α-Synuclein Fibrils Formed in the Absence and Presence of a Model Lipid Membrane: A Small and Wide-Angle X-Ray Scattering Study. *Front. Soft Matter* **2022**, *1*, No. 741996, DOI: 10.3389/frsfm.2021.741996.
(63) Hamley, I. W.; Castelletto, V. Small-Angle Scattering Techniques for Peptide and Peptide Hybrid Nanostructures and Peptide-Based Biomaterials. *Adv. Colloid Interface Sci.* **2023**, *318*, No. 102959.
(64) Shi, Y.; Xie, T.; Leach, D. G.; Wang, B.; Young, S.; Osman, A. A.; Sikora, A. G.; Ren, X.; Hartgerink, J. D.; Myers, J. N.; Rangel, R. Local Anti−PD-1 Delivery Prevents Progression of Premalignant Lesions in a 4NQO-Oral Carcinogenesis Mouse Model. *Cancer Prev. Res.* **2021**, *14* (8), 767−778.
(65) Kakiuchi, Y.; Hirohashi, N.; Murakami-Murofushi, K. The Macroscopic Structure of RADA16 Peptide Hydrogel Stimulates Monocyte/Macrophage Differentiation in HL60 Cells via Cholesterol Synthesis. *Biochem. Biophys. Res. Commun.* **2013**, *433* (3), 298−304.
(66) Sankar, S.; O'Neill, K.; Bagot D'Arc, M.; Rebeca, F.; Buffier, M.; Aleksi, E.; Fan, M.; Matsuda, N.; Gil, E. S.; Spirio, L. Clinical Use of the Self-Assembling Peptide RADA16: A Review of Current and Future Trends in Biomedicine. *Front. Bioeng. Biotechnol.* **2021**, *9*, No. 679525, DOI: 10.3389/fbioe.2021.679525.
(67) Yan, C.; Pochan, D. J. Rheological Properties of Peptide-Based Hydrogels for Biomedical and Other Applications. *Chem. Soc. Rev.* **2010**, *39* (9), 3528−3540.
(68) Wang, J.; Xie, T.; Wang, B.; William, W. N.; Heymach, J. V.; El-Naggar, A. K.; Myers, J. N.; Caulin, C. PD-1 Blockade Prevents the Development and Progression of Carcinogen-Induced Oral Premalignant Lesions. *Cancer Prev. Res.* **2017**, *10* (12), 684−693.
(69) Luo, L.; Yang, J.; Zhu, C.; Jiang, M.; Guo, X.; Li, W.; Yin, X.; Yin, H.; Qin, B.; Yuan, X.; Li, Q.; Du, Y.; You, J. Sustained Release of Anti-PD-1 Peptide for Perdurable Immunotherapy Together with Photothermal Ablation against Primary and Distant Tumors. *J. Controlled Release* **2018**, *278*, 87−99.
(70) Heremans, J.; Awad, R. M.; Bridoux, J.; Ertveldt, T.; Caveliers, V.; Madder, A.; Hoogenboom, R.; Devoogdt, N.; Ballet, S.; Hernot, S.; Breckpot, K.; Martin, C. Sustained Release of a Human PD-L1 Single-Domain Antibody Using Peptide-Based Hydrogels. *Eur. J. Pharm. Biopharm.* **2024**, *196*, No. 114183.
(71) Shi, Y.; Li, D.; He, C.; Chen, X. Design of an Injectable Polypeptide Hydrogel Depot Containing the Immune Checkpoint Blocker Anti-PD-L1 and Doxorubicin to Enhance Antitumor Combination Therapy. *Macromol. Biosci.* **2021**, *21* (6), No. 2100049.
(72) Nambiar, M.; Schneider, J. P. Peptide Hydrogels for Affinity-Controlled Release of Therapeutic Cargo: Current and Potential Strategies. *J. Peptide Sci.* **2022**, *28* (1), No. e3377.
(73) Liao, S.-M.; Du, Q.-S.; Meng, J.-Z.; Pang, Z.-W.; Huang, R.-B. The Multiple Roles of Histidine in Protein Interactions. *Chem. Cent. J.* **2013**, *7*, 44.